Supporting Information

Greatly Enhanced Energy Storage and Discharge Properties in $AgNbO_3$ Ceramics with Stable Antiferroelectric Phase and High Breakdown Strength Using Hydrothermally Synthesized Powders

Jie Huang[a], Xu Hou[b], Shuaibing Gao[a], Yuqi Zhou[a], Haitao Huang[c], Yunbin He[a,*], and Qingfeng Zhang[a,*]

[a]Hubei Key Lab of Ferro & Piezoelectric Materials and Devices, School of Materials Science & Engineering, Hubei University, Wuhan 430062, China

[b]Department of Engineering Mechanics, Zhejiang University, Hangzhou, Zhejiang 310027, China

[c]Department of Applied Physics, The Hong Kong Polytechnic University, Hong Kong, China

*Corresponding authors.

E-mails: ybhe@hubu.edu.cn (Y. He); zhangqingfeng@hubu.edu.cn (Q. Zhang)

Finite Element Method Modeling

In the phase field model for dielectric breakdown of ceramics, a scalar phase field $s(\mathbf{r}, t)$ is taken as the order parameter to describe the state of damage.[S1] The value of s varies from 0 to 1, with $s = 1$ indicating the un-breakdown state and $s = 0$ the fully breakdown state. Similar to that of brittle fracture,[S2] the temporal propagation of spatially breakdown path can be obtained from the following time-dependent Ginzburg Landau (TDGL) equation:

$$\frac{\partial s(\mathbf{r},t)}{\partial t} = -m\frac{\delta H}{\delta s(\mathbf{r},t)} \tag{S1}$$

where H is the total free energy of the ceramic system, which can be expressed by the integration of the electrical enthalpy h over the whole system volume V, t represents

time, m is the kinetic coefficient relating to the dielectric breakdown propagation, $\delta H/\delta s(\mathbf{r}, t)$ denotes the thermodynamic driving force, $\mathbf{r}$ is the spatial vector, and $\mathbf{r} = (x_1, x_2)$ for the two-dimensional simulation considered in this work. Generally speaking, the electrostatic energy is stored by the outer electrical loading and when exceeds the criterion for propagation, it will be released to provide the energy dissipation for creation of the damaged phase, i.e. conductive breakdown channel. The total free-energy density h of the material can be expressed as a function of order parameter s, its gradient ∇s, and electric field E_i:

$$h = h_{\text{elec}}(s, E_i) + h_{\text{dam}}(s) + h_{\text{grad}}(\nabla s) \tag{S2}$$

The electrostatic energy density $h_{\text{elec}}(s, E_i)$ can be described through the Legendre transform as:

$$h_{\text{elec}}(s, E_i) = -\frac{1}{2}\varepsilon E_i E_i \tag{S3}$$

where ε is the permittivity of material and the electric field components can be calculated by the negative gradient of electric potential $E_i = -\Phi_i$. Note that, the fully damaged channel after dielectric breakdown will lose its insulating capability and become conductive. To describe the conductive behavior of the fully damaged phase, it is considered as a dielectric phase with very large permittivity for simplicity.[S1] The permittivity of the system is written as a function of order parameter s,

$$\varepsilon(s) = \frac{\varepsilon^0}{f(s) + \eta} \tag{S4}$$

where ε^0 is the permittivity of the intact material, $f(s) = 4s^3-3s^4$ is the interpolation function selected to satisfy a smooth transition between the permittivity of damaged phase $\varepsilon(0)$ and undamaged phase $\varepsilon(1)$, η is a small enough number to realize the large

permittivity of damaged phase in the numerical calculation and η is selected to be 10^{-5} in this work. To evaluate the energy consumption for the creation of damaged phase, the breakdown energy density is then introduced,

$$h_{\mathrm{dam}}(s) = W_{\mathrm{c}}[1 - f(s)] \tag{S5}$$

with W_{c} indicating the critical electrostatic energy density for the formation of damaged phase. More detailed, $W_{\mathrm{c}} = \Gamma/l^2$, Γ is approximately the breakdown energy, and l is an intrinsic length scale of the breakdown channel. To include the contribution of interface between the damaged phase and undamaged phase, the gradient energy density is then introduced as

$$h_{\mathrm{grad}}(\nabla s) = \frac{\Gamma}{4}|\nabla s|^2 \tag{S6}$$

besides the TDGL equation, the Maxwell's equation of $\partial(-\partial h/\partial E_i)/(\partial x_i) = 0$ must be satisfied for the charge free material. The detailed expansions of the governing equations can be found in previous work.[S3] For convenience, the following set of the dimensionless variables are employed.

$$\phi^* = \frac{\phi}{\sqrt{(\frac{\Gamma}{\varepsilon^0})}}, t^* = \frac{t}{\frac{l^2}{m\Gamma}}, r^* = r/l \tag{S7}$$

To solve above governing equations in the real space, a non-linear multi-field coupling finite element method is adopted by using COMSOL software. The simulation model of ceramics are considered as composites of grain cores and grain boundaries, with detailed distribution extracted from real SEM images. Generally, the breakdown energy of the grain boundary is considered to be higher than that of the grain, while the permittivity of the grain boundary is degenerative. Subscript 'g'

represents grain cores and ‘gb’ is corresponding to grain boundaries. In this work, the breakdown energy is set as Γ_g/Γ_{gb} = 1/10, and the permittivity is taken as $\varepsilon_g/\varepsilon_{gb}$ = 10/1. The average size of the meshing block grids is approximately 34×34 nm^2 in the real space. Each node of meshes has 2 degrees of freedom, including 1 electrical potential and 1 breakdown order parameter. Periodic boundary condition was applied along the x_1 direction to describe the infinite size of the samples in plane. The distribution of initial state of breakdown order parameter is uniformly set as 1 for the intact phase. In order to concentrate the electric field and initiate breakdown in a controllable way, a thin stripe with initial s value set to be 0, is placed at the middle of the sample and connected to the top electrode. The loading of external electric filed was applied along the x_2 direction by giving specific electric potential on the top surface with the bottom surface grounded. The electric field is uniformly raised to E^* = 5 until t^* = 0.1, then kept constant.

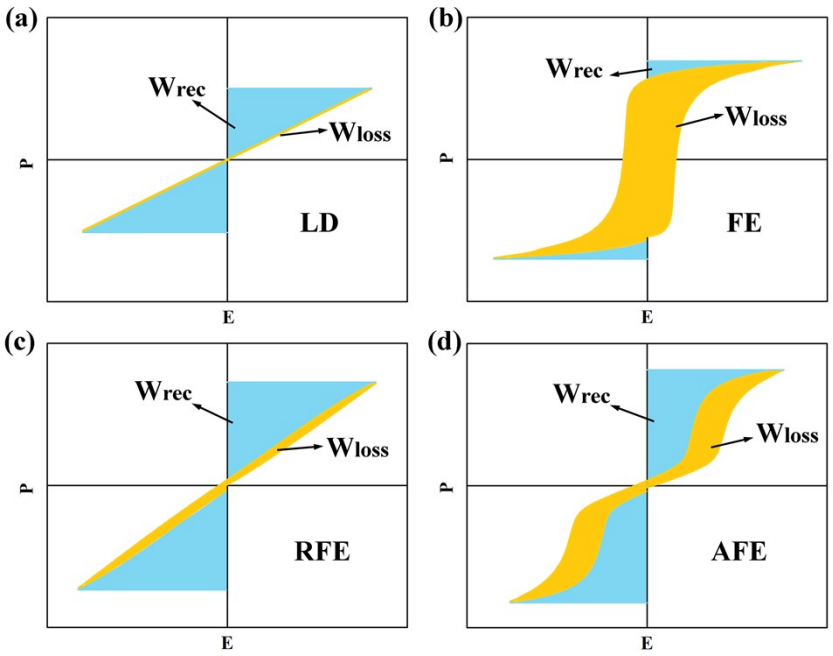

Fig. S1. Schematic diagram of *P-E* hysteresis loops, and some characteristic parameters for energy storage of (a) linear dielectrics, (b) ferroelectrics, (c) relaxor ferroelectrics, and (d) antiferroelectrics.

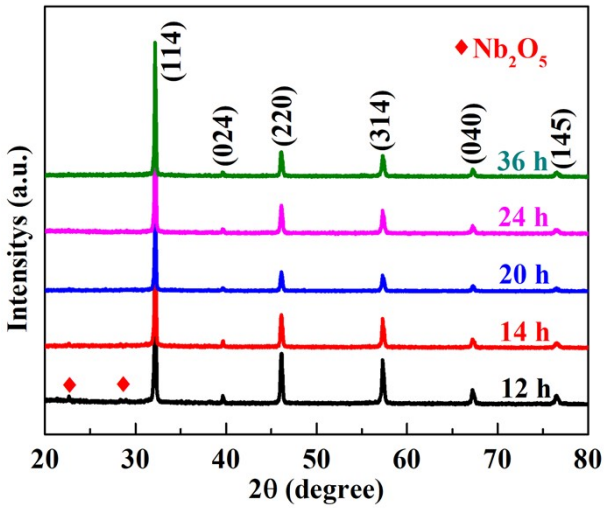

Fig. S2. XRD patterns of $AgNbO_3$ powders prepared by the hydrothermal method with different synthesis time.

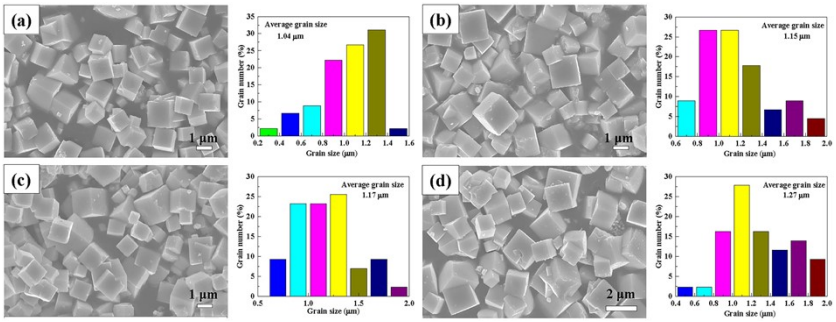

Fig. S3. FE-SEM images and the grain size distribution of $AgNbO_3$ powders prepared by the hydrothermal method with different synthesis time: (a) 14 h, (b) 20 h, (c) 24 h, and (d) 36 h.

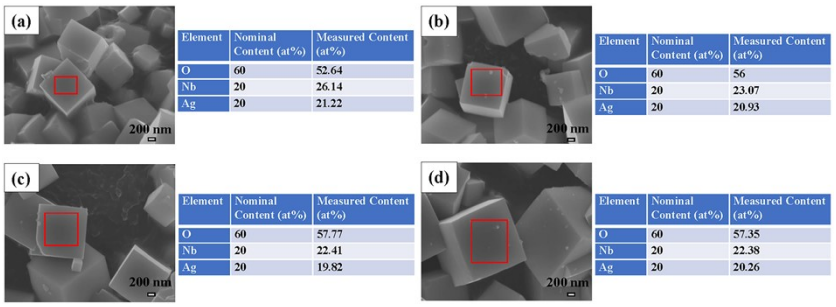

(a) Element	Nominal Content (at%)	Measured Content (at%)
O	60	52.64
Nb	20	26.14
Ag	20	21.22

(b) Element	Nominal Content (at%)	Measured Content (at%)
O	60	56
Nb	20	23.07
Ag	20	20.93

(c) Element	Nominal Content (at%)	Measured Content (at%)
O	60	57.77
Nb	20	22.41
Ag	20	19.82

(d) Element	Nominal Content (at%)	Measured Content (at%)
O	60	57.35
Nb	20	22.38
Ag	20	20.26

Fig. S4. EDS spectrum and quantitative atomic percent of various elements in hydrothermally prepared $AgNbO_3$ ceramics with different powder synthesis time: (a) 14 h, (b) 20 h, (c) 24 h, (d) 36 h.

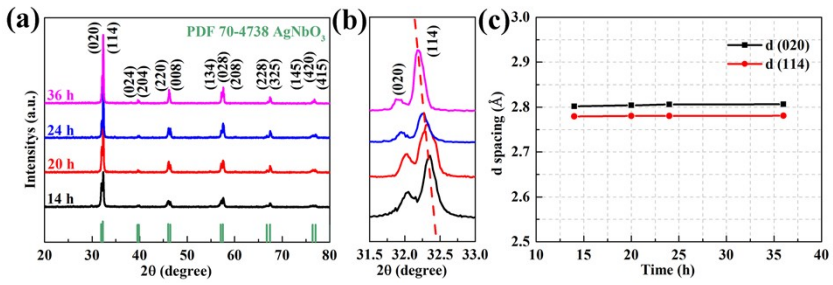

Fig. S5. (a) XRD patterns of $AgNbO_3$ ceramics prepared by the hydrothermal method with different powder synthesis time. (b) Fine scanning XRD patterns of the ceramics in the 2θ range of 31.5-33°. (c) The *d*-spacing for (020) and (114) planes.

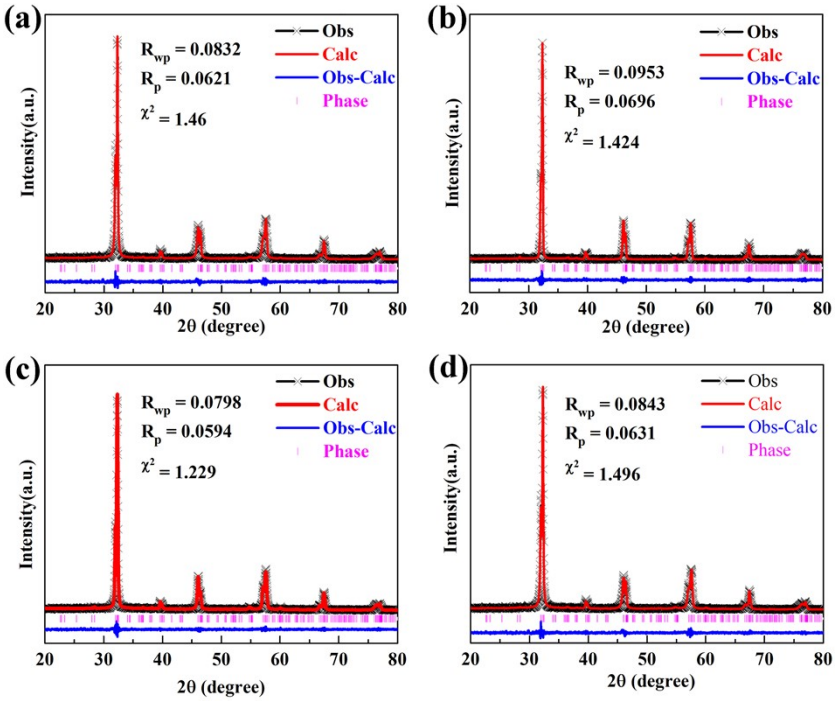

Fig. S6. Rietveld refinement on XRD patterns of $AgNbO_3$ ceramics prepared by the hydrothermal method with different powder synthesis time: (a) 14 h, (b) 20 h, (c) 24 h, and (d) 36 h based on *Pbcm* space group.

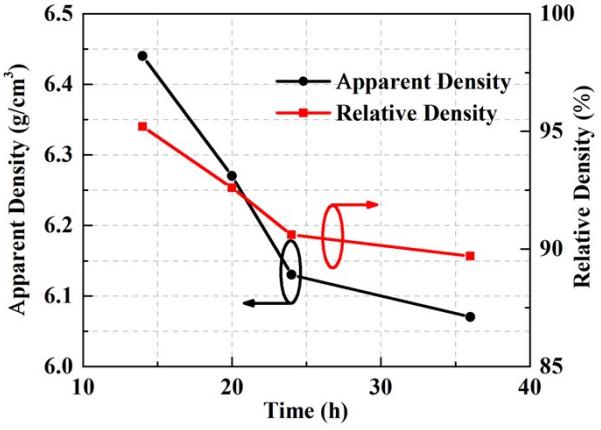

Fig. S7. Apparent and relative densities of $AgNbO_3$ ceramics prepared by the hydrothermal method with different powder synthesis time.

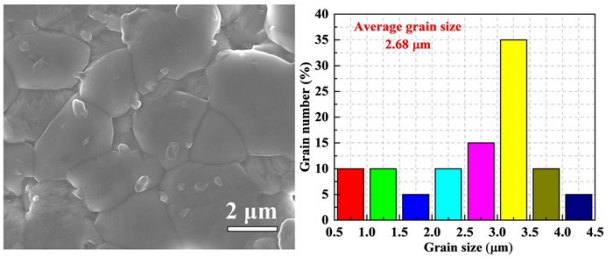

Fig. S8. The SEM image and grain size distribution of the $AgNbO_3$ ceramic prepared by the solid-state reaction method.

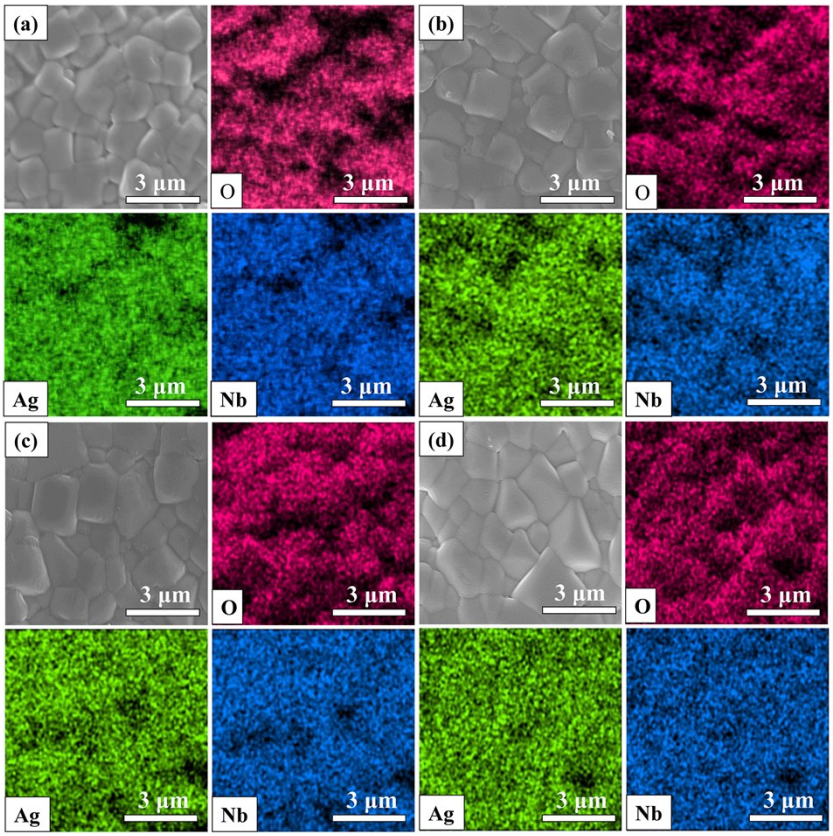

Fig. S9. FE-SEM-EDS mapping images of $AgNbO_3$ ceramics prepared by the hydrothermal method with different powder synthesis time: (a) 14 h, (b) 20 h, (c) 24 h, and (d) 36 h.

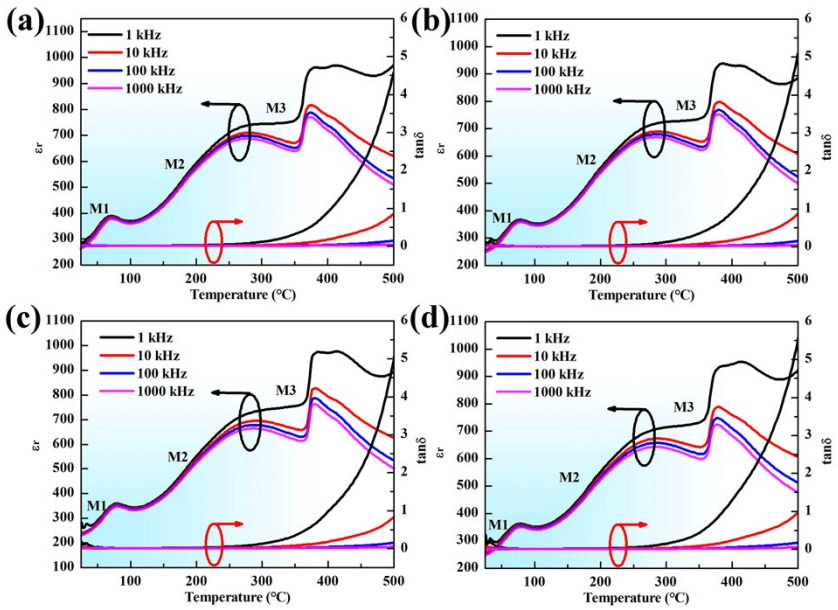

Fig. S10. Dielectric constant and loss of $AgNbO_3$ ceramics prepared by the hydrothermal method with different powder synthesis time: (a) 14 h, (b) 20 h, (c) 24 h, and (d) 36 h.

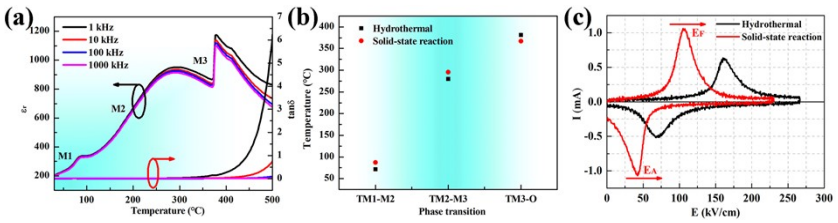

Fig. S11. (a) Dielectric constant and loss of the $AgNbO_3$ ceramic prepared by the solid-state reaction method. (b) Phase transition temperature and (c) unipolar *I-E* loops of $AgNbO_3$ ceramics prepared by the solid-state reaction way and hydrothermal way with powder synthesis time of 20 h.

(a)

	Nb-O1	Nb-O2	Nb-O3	Nb-O3'	Nb-O4	Nb-O4'	$\overline{\text{Nb-O}}$
Hydrothermal	2.006	1.972	1.874	2.165	2.038	1.937	1.998667
Solid-state reaction	2.14	1.994	1.926	2.002	2.018	1.974	2.009

(b)

	|O-O|c	|O-O|ab	|O-O|ba	|O-O|	|O-O|	|O-O|	|O-O|	$\overline{\text{O-O}}$
Hydrothermal	3.927	3.81	4.202	2.948	2.825	2.808	2.765	2.8365
Solid-state reaction	4.013	3.248	4.681	2.886	2.857	2.842	2.81	2.84875

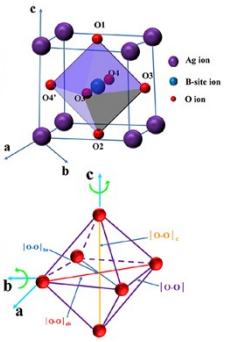

Fig. S12. (a) |Nb-O| bond and (b) |O-O| bond lengths of $AgNbO_3$ ceramics prepared by the solid-state reaction way and hydrothermal way with powder synthesis time of 20 h.

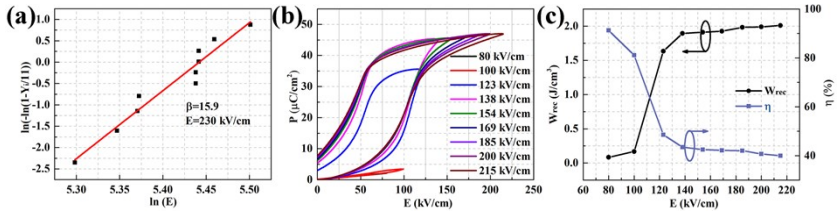

Fig. S13. (a) Weibull distribution plots, (b) unipolar *P-E* loops under different electric fields and (c) W_{rec} and η of the $AgNbO_3$ ceramic prepared by the solid-state reaction method**.**

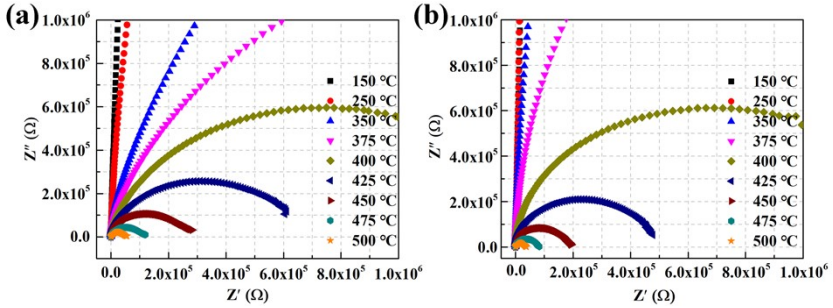

Fig. S14. Complex impedance plots of $AgNbO_3$ ceramics prepared by the (a) hydrothermal way with powder synthesis time of 20 h and (b) solid-state reaction method.

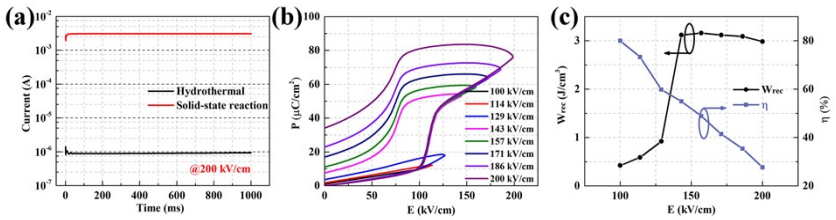

Fig. S15. (a) Leakage current densities of $AgNbO_3$ ceramics prepared by the solid-state reaction way and hydrothermal way with powder synthesis time of 20 h. (b) Unipolar *P-E* loops, and (c) W_{rec} and η of the $AgNbO_3$ ceramic prepared the solid-state reaction method at 160 °C.

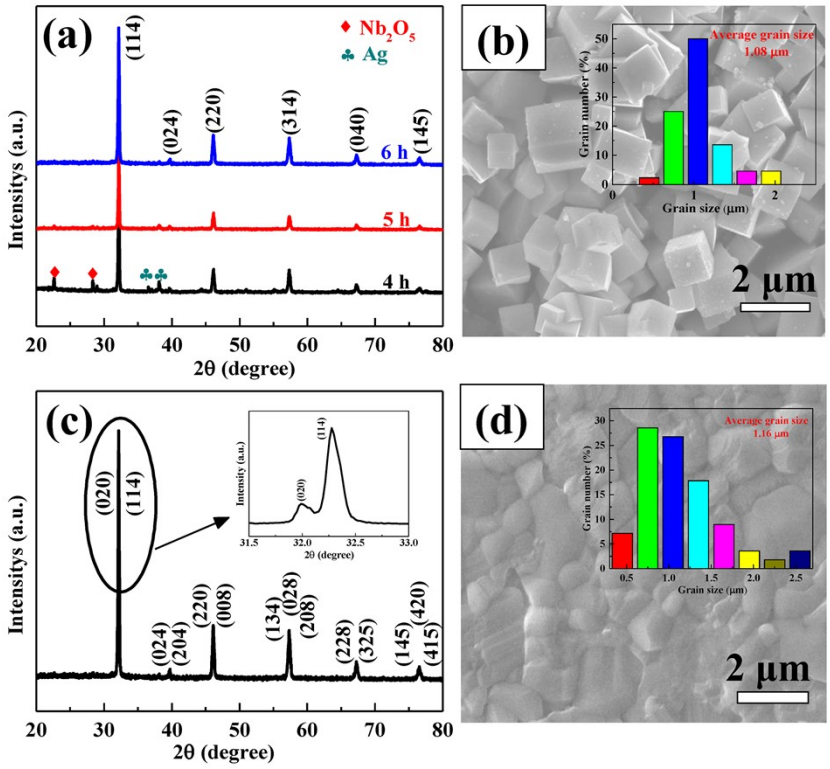

Fig. S16. (a) XRD patterns of $AgNbO_3$ powders prepared by the microwave-assisted hydrothermal method with different powder synthesis time, and (b) FE-SEM images and grain size distribution (the inset) of the powders with the synthesis time of 6 h. (c) XRD patterns of the microwave-assisted hydrothermally prepared $AgNbO_3$ ceramics with powder synthesis time of 6 h and (d) SEM images and grain size distribution (the

inset) of the ceramic.

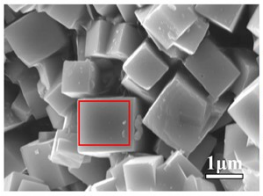

Element	Nominal Content (at%)	Measured Content (at%)
O	60	56.45
Nb	20	20.35
Ag	20	23.2

Fig. S17. EDS spectrum and quantitative atomic percent of various elements in $AgNbO_3$ ceramics prepared by the microwave-assisted hydrothermal method with powder synthesis time of 6 h.

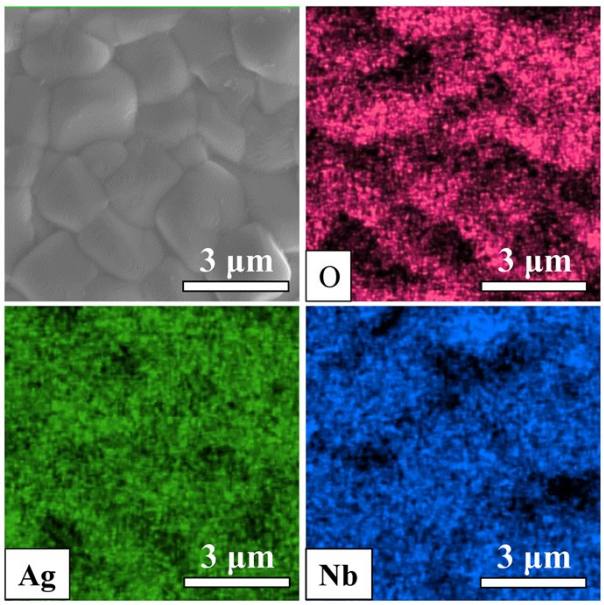

Fig. S18. FE-SEM-EDS mapping images of the $AgNbO_3$ ceramic prepared by the microwave-assisted hydrothermal method with powder synthesis time of 6 h.

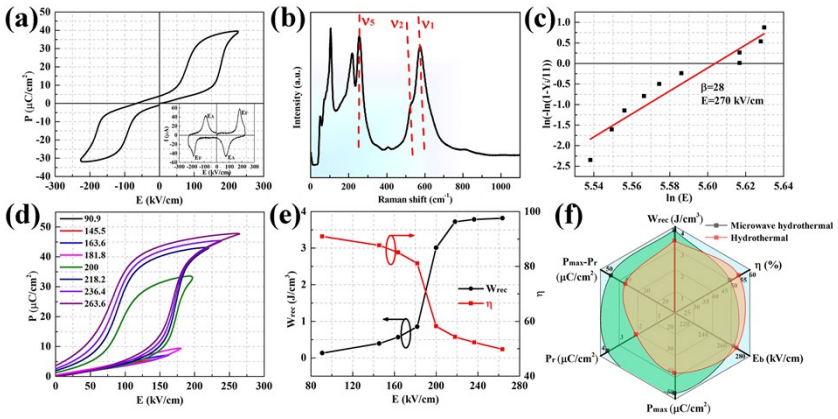

Fig. S19. (a) Unipolar *P*-*E* loops, (b) P_{max}, P_r and P_{max}-P_r, and (c) W_{rec} and η of $AgNbO_3$ ceramics prepared by the microwave-assisted hydrothermal method with powder synthesis time of 6 h during 10-350 Hz. (d) Unipolar *P*-*E* loops, (e) P_{max}, P_r P_{max}-P_r, and (f) W_{rec} and η of the ceramic under different cycle numbers and 100 Hz.

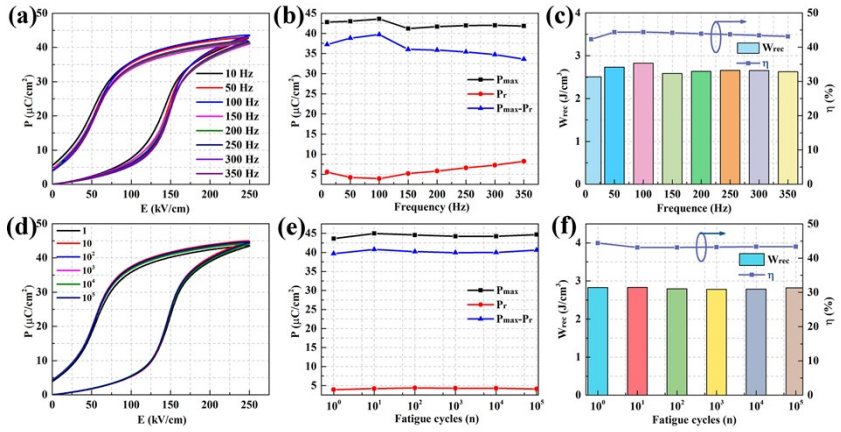

Fig. S20. (a) Bipolar *P*-*E* and *I*-*E* (the inset) loops, (b) Raman spectra, (c) Weibull distribution plots, (d) unipolar *P*-*E* loops at different electric fields, and (e) W_{rec} and η of the $AgNbO_3$ ceramic prepared by the microwave-assisted hydrothermal method with powder synthesis time of 6 h. (f) Comprehensive capacitive performance parameters of $AgNbO_3$ ceramics prepared by microwave-assisted hydrothermal and hydrothermal methods.

References

S1 K.C. Pitike and W. Hong, *J. Appl. Phys.,* 2014, **115,** 044101.

S2 V. Hakim and A. Karma, *J. Mech. Phys. Solids,* 2009, **57,** 342-368.

S3 Z.M. Cai, X.H. Wang, B.C. Luo, W. Hong, L.W. Wu and L.T. Li , *J. Am. Ceram. Soc.,* 2018, **101,** 1607-1615.